

Thermal and Vibrationally Activated Decomposition of the syn-CH₃CHOO Criegee Intermediate

Meenu Upadhyay and Markus Meuwly*

*Department of Chemistry, University of Basel, Klingelbergstrasse 80 , CH-4056 Basel,
Switzerland.*

E-mail: m.meuwly@unibas.ch

June 25, 2021

Abstract

The full reaction pathway between the syn-CH₃CHOO Criegee Intermediate via vinyl hydroxyperoxide to OH+CH₂COH is followed for vibrationally excited and thermally prepared reactants. The rates from vibrational excitation are consistent with those found from experiments and tunneling is not required for reactivity at all initial conditions probed. For vibrationally excited reactant, VHP accumulates and becomes a bottleneck for the reaction. The two preparations - relevant for laboratory studies and conditions in the atmosphere - lead to a difference of close to one order of magnitude in OH production ($\sim 5\%$ vs. 35%) on the 1 ns time scale which is an important determinant for the chemical evolution of the atmosphere.

The hydroxyl radical (OH), one of the most powerful oxidizing agents, plays an important role in the chemical evolution of the atmosphere.¹ OH, also referred to as the “detergent of the troposphere”,^{2,3} triggers degradation of many pollutants including volatile organic compounds (VOCs) and is an important chain initiator in most oxidation processes in the atmosphere. The amount of OH generated from alkene ozonolysis is an important determinant required for chemical models of the lower atmosphere. Field studies have suggested that ozonolysis of alkenes is responsible for the production of about one third of the atmospheric OH radicals during daytime, and is the predominant source of OH radicals at night.^{4,5} Alkene ozonolysis proceeds through a 1,3-cycloaddition of ozone across the C=C bond to form a primary ozonide which then decomposes into carbonyl compounds and energized carbonyl oxides, known as Criegee Intermediates (CIs).⁶ These highly energized intermediates rapidly undergo either unimolecular decay to hydroxyl radicals⁷ or collisional stabilization.⁸ Stabilized Criegee intermediates can isomerize and decompose into products including the OH radical, or undergo bimolecular reactions with water vapor, SO₂, NO₂ and acids.^{9,10} The high energy and short lifetime of these zwitterionic species complicates their direct experimental

characterization.

One of the smallest CIs that can either follow unimolecular decay to generate OH or bimolecular reactions under atmospheric conditions is the acetaldehyde oxide (CH_3CHOO). This species is generated from ozonolysis of trans-2-butene.¹¹ Unimolecular decomposition of stabilized *syn*- CH_3CHOO proceeds through a five membered transition state with an energy barrier of ~ 17 kcal/mol,¹²⁻¹⁴ following 1,4- hydrogen transfer to form vinyl hydroperoxide (VHP). Subsequent homolytic cleavage of the $\text{O}_\text{A}-\text{O}_\text{B}\text{H}$ bond (see Figure 1A) leads to OH and vinoxy radical.¹⁵ Conversely, starting from the *anti*- CH_3CHOO isomer, the main product is methyl-dioxirane which proceeds through a ring-closure step.¹⁶ The conversion of the *syn*- to the *anti*-isomer involves a barrier of ~ 42 kcal/mol which makes such a reorganization highly unlikely.¹⁷

Direct time-domain experimental rates, for appearance of OH from unimolecular dissociation of *syn*- CH_3CHOO under collision free conditions were obtained by vibrationally activating the molecules at specific energies in the vicinity of¹⁸ and below¹⁹ the transition state barrier of 1,4 hydrogen transfer. Statistical RRKM²⁰ rates with tunneling and zero point energy correction agreed with experimentally determined OH formation rates at energies in the vicinity of the barrier (~ 6000 cm^{-1}). Experiments on deuterated *syn*- CD_3CHOO found a kinetic isotope effect of ~ 50 for unimolecular decay at energies near the barrier which suggests that tunneling occurs.²¹ Later computational work reported the possibility for rearrangement of the vinoxy and hydroxyl radical to form hydroxyacetaldehyde instead of O-O bond homolysis in VHP.²² The dynamics of energized *syn*- CH_3CHOO from simulations initiated at the TS towards VHP reported prompt OH-dissociation without visiting VHP along the pathway.²³ Finally, thermal unimolecular decay is also a relevant pathway for *syn*- CH_3CHOO loss in the atmosphere with rates at room temperature of 100 to 300 s^{-1} .^{24,25}

The second step for OH formation is O–O cleavage starting from VHP which converts singlet VHP into two doublet radicals (OH and CH₂COH).²⁶ At the MP2 level of theory reported electronic energy differences between VHP and the dissociation products of 31.5 kcal/mol and 35.8 kcal/mol using the 6-31G(d) and aug-cc-pVTZ basis sets, respectively.²⁶ Calculations at the multi-reference configuration interaction singles and doubles (MRCISD) level of theory report dissociation energies between 14.3 and 17.8 kcal/mol depending on the basis set used. However, as the asymptotic energy differences appear to depend both, on the size of the active space and the basis set used, a definitive dissociation energy for this process is currently not available. In another, more recent effort²⁷ the PES for the OH elimination reaction was determined at the CASPT2(12,10)/cc-pVDZ level of theory which find a first submerged barrier, 23.0 kcal/mol above VHP, and the second, “positive barrier”, 29.3 kcal/mol above VHP. Both of them connect to the same asymptotic state (CH₂COH+OH) which is 27.2 kcal/mol above the VHP energy.

For the *syn*-CH₃CHOO → VHP → CH₂COH + OH reaction it has been suggested that the first step - 1,4-hydrogen shift - is rate limiting, followed by a rapid homolysis of the O–O bond.^{15,26,28} On the other hand, there has also been evidence that VHP itself is a significant bottleneck along the reaction coordinate.²⁹ This view is supported by the notion that with an estimated O–O bond energy of ~ 19 kcal/mol thermal decomposition of VHP would require a unimolecular rate below 10⁹ s⁻¹ which is not consistent with simple scission.²⁹ Hence, there is also uncertainty on the question which - if any - of the two steps is clearly rate limiting.

For a more atomistically resolved understanding of the entire pathway *syn*-CH₃CHOO → CH₂CHOOH → CH₂CHO+OH, a statistically significant number of reactive trajectories based on full-dimensional reactive potential energy surfaces is run and analyzed in the present work. For this, reactive MD simulations are carried out based on an empirical multisurface adiabatic reactive PES (using CHARMM³⁰) and a neural network-based PES using the

atomic simulation environment (ASE)³¹ for comparison.

Results and Discussion

The Interaction Potentials The quality of the MS-ARMD and PhysNet representations of the reactive PESs is reported in Figures 1B and C. For MS-ARMD the fitted PESs for the reactant (blue, CH₃CHOO) and the product (green, VHP) states have overall root mean squared errors (RMSEs) of 1.1 kcal/mol and 1.2 kcal/mol, typical for such an approach.³²⁻³⁴ The IRC closely follows the reference MP2 calculations, see inset Figure 1B, which underlines the quality of the reactive PES. For OH-elimination a conventional Morse fit to the reference MP2 calculations was used with $r_e^{\text{OO}} = 1.45 \text{ \AA}$, $D_0^{\text{OO}} = 31.5 \text{ kcal/mol}$, and $\beta = 2.3 \text{ \AA}^{-1}$. However, because O–O bond breaking may involve multi-reference character^{26,27} simulations with a value of $D_e^{\text{OO}} = 23.5 \text{ kcal/mol}$ were also carried out, consistent with findings from CCSD(T)-F12b/CASPT2 calculations.²⁷

The quality of the PhysNet representation of the global reactive PES is reported in Figure 1C. Here, the mean average error on the test set (~ 10000 structures not used for training or validation) is 0.02 kcal/mol with a RMSE of 0.19 kcal/mol and $R^2 = 1 - 10^{-7}$. Again, this performance is in line with previous work.³⁵⁻³⁷

As a first exploration of the PES the minimum dynamic path (MDP) for the 1,4 hydrogen shift reaction was determined on the PhysNet PES, see Figure S2. Starting from the initial structure “A”, this reaction passes through a five-membered ring (structure “C”) before formation of VHP (structure “E”).

A Typical Reactive Trajectory An illustrative example for a reactive trajectory from

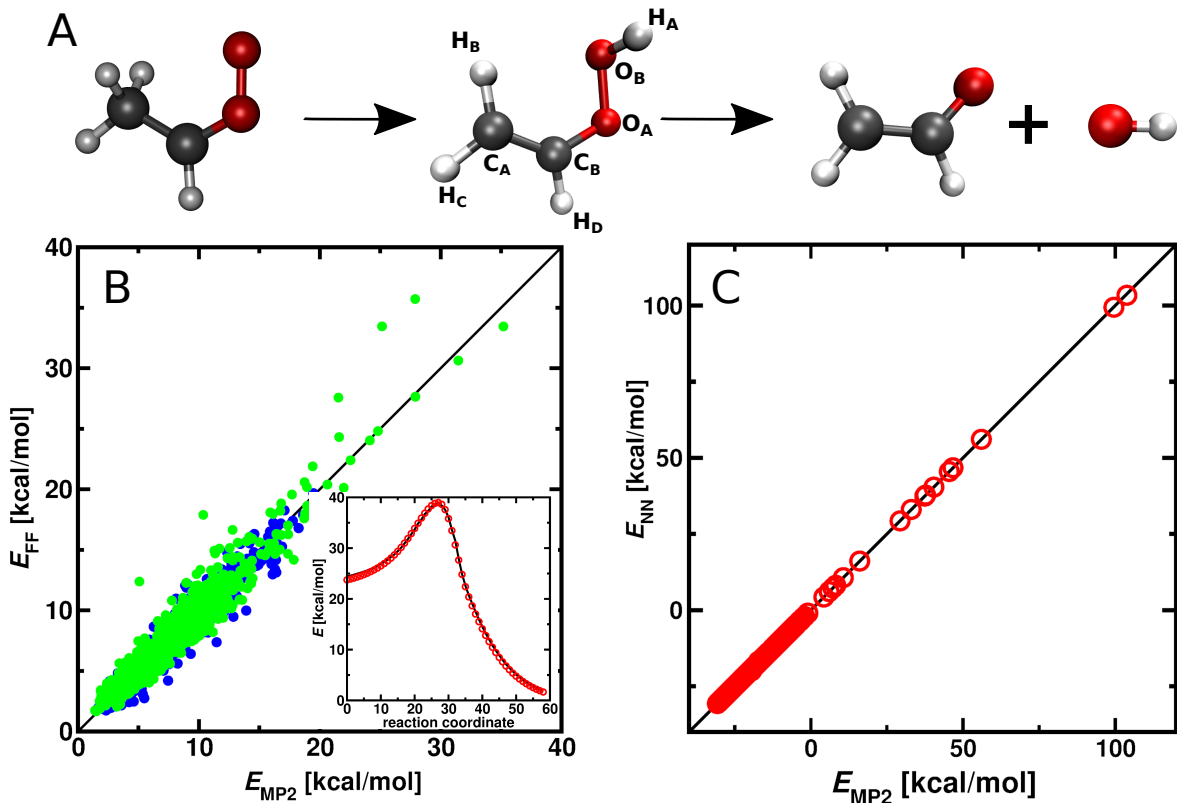


Figure 1: Quality of the PESs. Panel A: Schematic representation of OH formation starting from the *syn*-CH₃CHOO Criegee intermediate (left) via vinyl hydroperoxide (VHP, middle) through a 1,4 hydrogen shift reaction and subsequent OH-elimination to yield vinyloxy radical + OH (right). Panel B: Correlation of 1612 *ab initio* reference structures and the fitted force field for reactant (blue) and product (green) with RMSE value of 1.1 kcal/mol and 1.2 kcal/mol respectively. Inset: *ab initio* IRC (red circles) and fitted MS-ARMD (black curve). Panel C: Correlation between reference (MP2) and predicted (PhysNet) energies. The 10540 test set structures are predicted with MAE of 0.02 kcal/mol and RMSE of 0.19 kcal/mol.

MS-ARMD simulations is reported in Figure 2A. Here, the C_AH_A, O_BH_A, and O_AO_B time series are shown (for labeling see Figure 1A) which are directly relevant to the reaction. Initially, the C_AH_A separation (black trace in Figure 2A) fluctuates around 1.12 Å which is close to the equilibrium bond length, and the O_BH_A separation is large (ranging from 2 to 4 Å) as the system is in its reactant state. Such large variations are elicited by the CH₃ rotation. At $t \sim 0.5$ ns the 1,4 hydrogen shift reaction occurs which increases the C_AH_A and O_AO_B separations and shortens the O_BH_A bond due to bond formation. For the next ~ 0.3 ns the system is in its VHP state before OH elimination takes place at $t \sim 0.79$ ns following

breaking of the $O_A O_B$ bond.

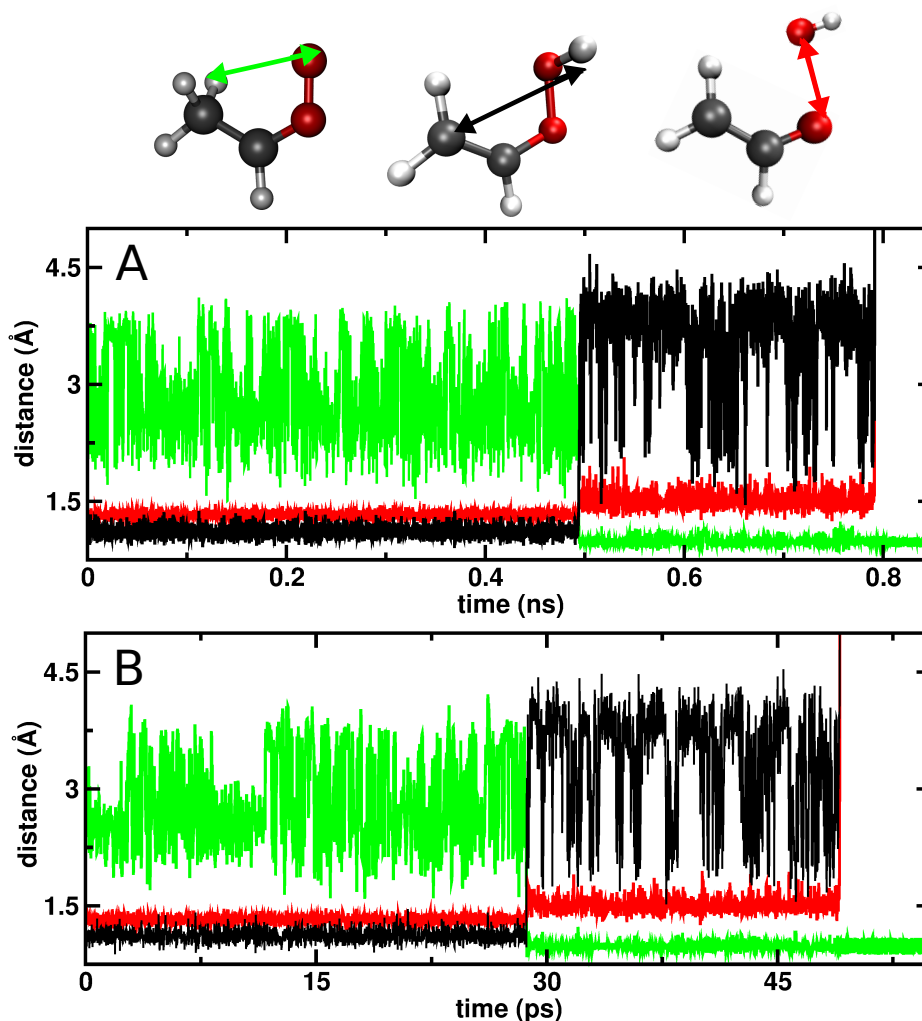


Figure 2: Time series for different distances for the reaction $syn\text{-CH}_3\text{CHOO} \rightarrow \text{VHP} \rightarrow \text{CH}_2\text{CHO} + \text{OH}$. Panel A: using MS-ARMD simulations at $t \sim 0.5$ ns VHP forms and at $t \sim 0.79$ ns OH elimination takes place. Panel B: using PhysNet at $t \sim 28$ ps VHP forms and at $t \sim 47$ ps OH elimination takes place. Black, red, and green solid lines correspond to the $C_A H_A$, $O_A O_B$, and $O_B H_A$ distances, respectively.

A similar trajectory, run with ASE and the PhysNet representation, is shown in Figure 2B. Again, CH_3 rotation is found. As for the MS-ARMD simulations, for VHP (between $t \sim 28$ ps and $t \sim 47$ ps) the position of the OH-group switches between *syn*- and *anti*-conformers, respectively. These lead to long and short $C_A\text{-}H_A O_B$ separations (black trace).

The Vibrationally Assisted Reaction In laboratory-based experiments^{18,27} the reaction path following *syn*-CH₃CHOO → VHP → CH₂CHO+OH is initiated by excitation of the CH stretch vibration of the terminal CH₃ group with energies ranging from ~ 5600 cm⁻¹ to ~ 6000 cm⁻¹. This corresponds to about 2 quanta in the methyl-CH stretch mode. In the simulations, excitation of this mode was accomplished by scaling the velocities^{33,38} along the CH-local mode. Equilibrium simulations for *syn*-CH₃CHOO were carried out at 300 K and 50 K to generate the initial ensemble. It should, however, be noted that “temperature” as determined from the equivalence of kinetic energy and $3/2Nk_{\text{B}}T$, as is usually done in MD simulations,³⁹ should not be directly compared with experimentally reported temperatures (e.g. 10 K rotational temperature in Ref.¹⁸).

Simulations were run using the same internal energies as those reported from experiments, i.e. [5603, 5709, 5748, 5818, 5951, 5984, 6082] cm⁻¹. For each energy $N_{\text{tot}} = 10000$ individual trajectories were run. The ensuing rates were determined from following the number $N(t) = 1 - N_{\text{OH}}$, i.e. counting those that had not reached the OH-elimination product, see Table S1 and S2 and fitting $N(t)$ to either a single ($\sim \exp(-kt)$) or a stretched-exponential ($\exp(-kt)^\gamma$) dependence (see Figure S3).⁴⁰ The rates k as a function of excitation energy are reported in Figure 3A together with those from experiment (red symbols).¹⁸

MS-ARMD simulations from an ensemble generated at 300 K were carried out for two values of the O–O dissociation energy, see above. Rates from simulations with $D_e^{\text{OO}} = 31.5$ kcal/mol (green) and $D_e^{\text{OO}} = 23.5$ kcal/mol (black) are shown in Figure 3A. Depending on the value of D_e^{OO} the rates differ by a factor of ~ 10 but following a similar energy dependence, consistent with that observed in the experiments. Bootstrapping is used to determine statistical errors by randomly sampling 8000 trajectories 30 times from all 10000 trajectories at each energy. The error bars due to parameter uncertainties in the fitting of $\ln N(t)/N(0)$ vs. time are a factor of 4 to 10 smaller than those from bootstrapping.

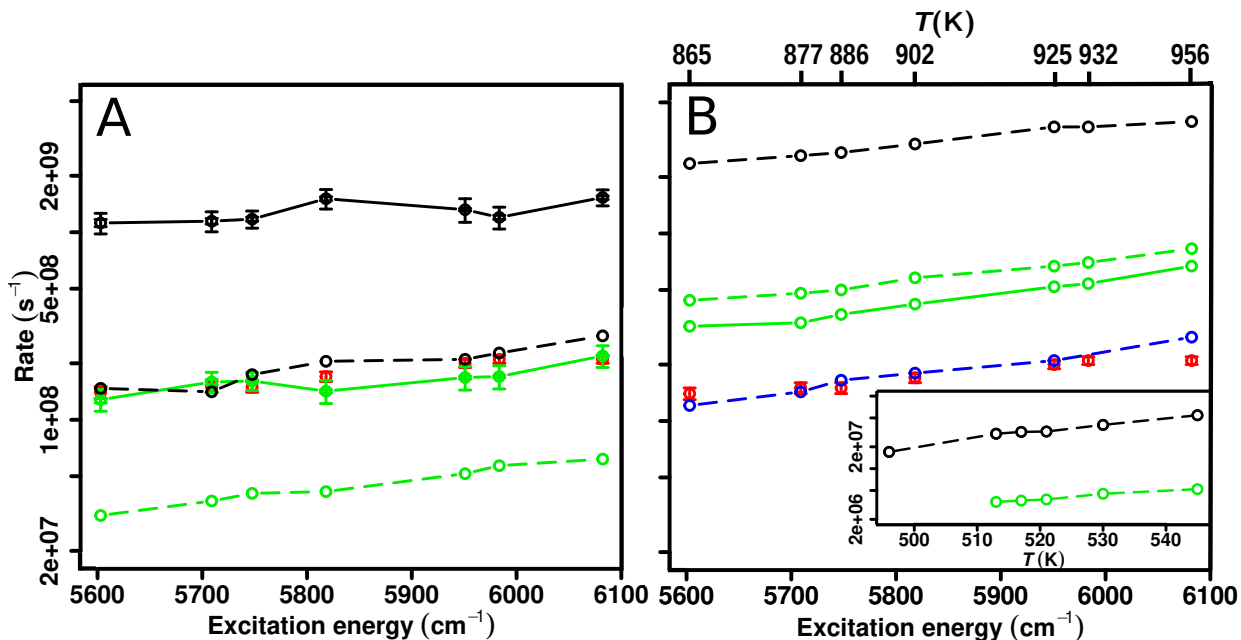


Figure 3: OH formation rates from vibEX and thermal simulations. Panel A: Rates from MS-ARMD simulations following excitation of the $C_A H_A$ stretch vibration (vibEX) at different excitation frequencies. The green and black lines are for $D_e^{OO} = 31.5$ kcal/mol (consistent with the present and earlier²⁶ MP2 calculations), and $D_e^{OO} = 23.5$ kcal/mol respectively. The red points with error bars are the experimental results. Solid and dashed lines are rates from fitting $N(t)/N_{tot}$ to stretched or single exponentials, respectively, with separate error bars from bootstrapping and for the parameters. Panel B: Rates from thermal simulations using MS-ARMD (identical color code as in panel A), and from PhysNet (dashed blue line). The top y -axis gives the temperature T as determined from $T = 2E_{kin}/(3Nk_B)$. The inset reports results from simulations at somewhat lower temperatures.

To assess the sensitivity of the results to the initial preparation of the system, vibEX dissociation simulations were also carried out by sampling from an ensemble generated at 50 K using MS-ARMD and $D_e^{OO} = 23.5$ kcal/mol. Several 1000 simulations were run for 5 ns at different excitation energies. At 5603 cm⁻¹ 15 out of 2000, 5747 cm⁻¹ 23 out of 1000, 5818 cm⁻¹ 6 out of 400 show VHP formation. Hence, reactivity is also found for considerably lower (thermal) energies but the rates are slower than those started from the ensemble generated at 300 K. However, a larger number of trajectories would be required for better converged rates.

The Thermal Reaction In the atmosphere, vibrational excitation is not the likely pri-

mary mechanism by which *syn*-CH₃CHOO is energized. Rather, the ozonolysis reaction is expected⁴¹ to lead to a “warm” or “hot” parent molecule (*syn*-CH₃CHOO) which subsequently decays following the 1,4 hydrogen shift and O–O dissociation reactions.^{29,42,43} Hence, “thermal” simulations were also carried out by heating the reactant to average temperatures between 865 K and 956 K, commensurate with internal energies of ~ 5500 to 6000 cm^{-1} . Again, the equivalence between “temperature” and “kinetic energy” is rather qualitative. For this reason, additional simulations at somewhat lower temperatures (500 K to 550 K) were also carried out and analyzed.

The rates were determined by following $N(t)$, see Tables S3, S4 and S5. For these “thermal” simulations with $D_e^{\text{OO}} = 31.5 \text{ kcal/mol}$, $N(t)$ is well represented by a single exponential decay for times $t < 200 \text{ ps}$ whereas a stretched exponential is again required for longer simulation times, see Figure S4. Such information is of particular relevance in the context of *ab initio* MD simulations which can usually only be carried out on the multiple $\sim 10 \text{ ps}$ time scale for sufficiently high-level treatments of the electronic structure.⁴⁴

Thermal rates from ~ 9000 independent simulations using the MS-ARMD (solid green and black lines) and PhysNet (dashed blue line) representations are reported in Figure 3B. MS-ARMD simulations were run for the same two values of the O–O dissociation energy as the vibEX simulations with rates ranging from 3×10^8 to $5 \times 10^9 \text{ s}^{-1}$. The temperature dependence is moderate and follows that found from experiments using vibrational excitation although the magnitude of the computed rate is consistently higher by a factor of 5 to 10. Thermal rates from simulations using PhysNet show the same temperature dependence as the one observed in experiments and from MS-ARMD simulations but with an amplitude that is closer to that from experiment ($\sim 10^8 \text{ s}^{-1}$). Exploring effects due to a change in D_e^{OO} is not easily accomplished using PhysNet because the underlying data set used in the fitting would need to be modified accordingly.

MS-ARMD simulations were also carried out for ensembles generated at lower temperatures, see inset Figure 3. As expected, the rates decrease by about an order of magnitude but remain consistent with experiment, exhibiting a comparable temperature dependence.

Analysis of the Reactive Trajectories With a statistically significant number of reactive trajectories ($\sim 10^4$) it is also possible to carry out additional analyses. Distributions of H-transfer and OH-formation times from vibEX and thermal MS-ARMD simulations are reported in Figure 4. Reactions initiated from vibrational excitation have a comparatively flat reaction time distribution up to ~ 0.2 ns for the 1,4 H-shift reaction, red histogram in Figure 4A. The reaction time is defined by the time interval between the point of vibrational excitation and VHP formation for which a geometrical criterion was used (O-H separation < 1.6 Å and O-O separation < 2.8 Å). For longer simulation times (> 0.2 ns) the reaction probability decays towards zero. Decay to $\text{CH}_2\text{COH}+\text{OH}$ in the vibEX simulations is delayed and the number of trajectories reaching the final state compared with those that complete the first step (1,4 H-shift) depends on time. For lower excitation energy (top panel in Figure 4A) appreciable OH elimination only starts after ~ 0.2 ns and does not reach more than 10 % of the amount of VHP formed on the 1 ns time scale. For higher excitation energies, the onset of OH elimination shifts to shorter times and the amount of OH formed increases in proportion. The fraction of VHP intermediates formed ranges from 74 % to 87 % compared with a fraction of 3 % and 7 % for the amount of OH formed from vibEX simulations (5603 cm^{-1} to 6082.2 cm^{-1}). Therefore, an appreciable amount of VHP accumulates on the 1 ns time scale and reacts to the OH-elimination product on longer time scales.

The situation changes considerably for the thermal reaction, see Figure 4B. Here, the reaction time distributions for the 1,4 H-shift reaction approach an exponential decay with simulation time for all temperatures considered. Similarly, the amount of OH formed follows

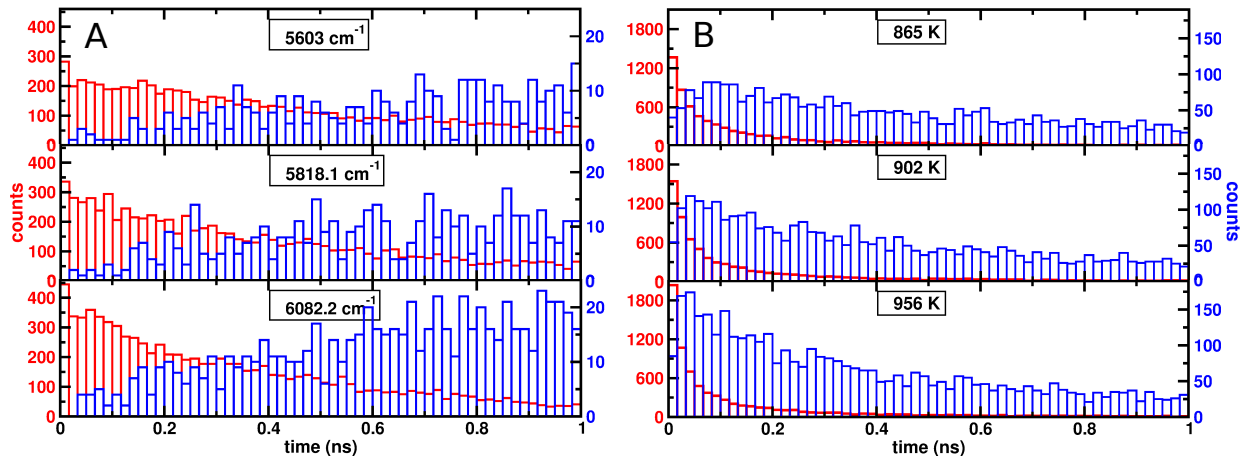


Figure 4: Distribution of reaction times for 1,4 H-shift [$\text{CH}_3\text{CHOO} \rightarrow \text{VHP}$, red] and OH-formation [$\text{CH}_3\text{CHOO} \rightarrow \text{CH}_2\text{COH} + \text{OH}$, blue] from vibEX (Panel A) and thermal (Panel B) simulations at different energies and temperatures using MS-ARMD with $D_e^{\text{OO}} = 31.5$ kcal/mol. Note that scales for the 1,4 H-shift distribution times are along the left hand y -axis and those for the total reaction time are along the right hand y -axis and that the magnitudes differ between panels A and B.

this. With increasing temperature (internal kinetic energy) the amount of VHP formed increases by about 50 % between 865 K and 956 K and the amount of OH formed by almost a factor of two. The fraction of VHP intermediates formed ranges from 73 % to 76 % compared with a fraction of 28 % and 38 % for the amount of OH formed.

The results from Figure 4 indicate that the VHP intermediate has a broad distribution of lifetimes, see Figure S6. As the probability to form VHP in the vibEX simulations has not reached zero within 1 ns (red distribution Figure 4A), VHP can also be generated on longer time scales from trajectories that have undergone more extensive internal vibrational energy redistribution (IVR). For the thermal trajectories the probability to form VHP has decayed to very low levels within 1 ns (Figure 4B). Thus, the VHP lifetime distributions in Figure S6 are expected to be close-to-converged. Importantly, vibrational excitation leads to about one order of magnitude less OH product than thermal preparation of the system at a similar internal energy.

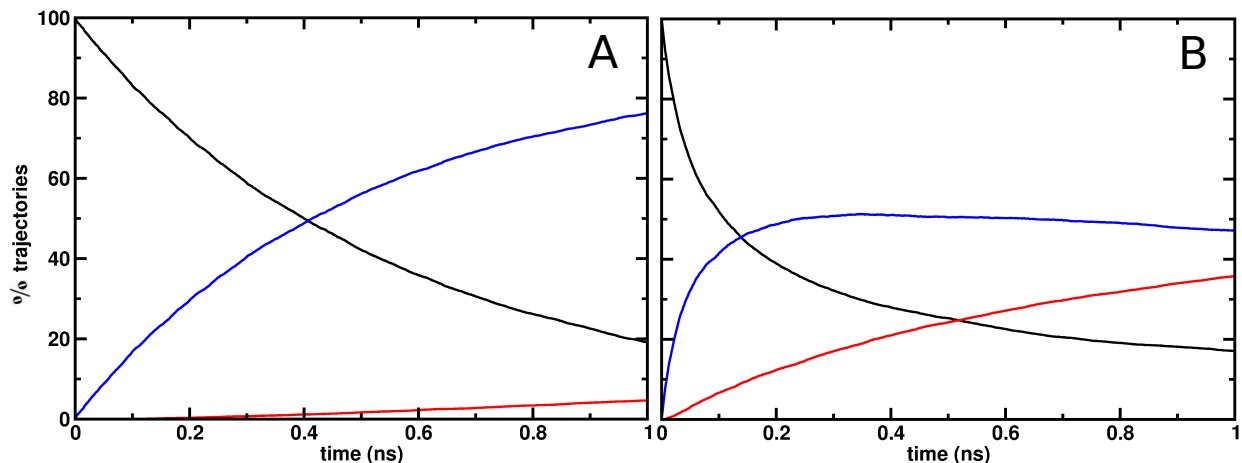


Figure 5: Change in concentration (in %) of Criegee Intermediate, VHP and $\text{CH}_2\text{COH}+\text{OH}$ as a function of time using MS-ARMD and $D_e^{\text{OO}} = 31.5$ kcal/mol. Panel A: from vibEX simulations at 5818.1 cm^{-1} . Panel B: from thermal simulations at 902 K for N_{Criegee} (black), N_{VHP} (blue), and N_{OH} (red), respectively. For vibEX the rate limiting step is the OH-elimination step whereas for thermal excitation none of the two steps is a clear reaction bottleneck. With comparable energy content in the reactant, thermal simulations yield close to one order of magnitude more OH-product than vibrational excitation of the methyl-CH-stretch.

Formation of the VHP intermediate follows different time traces depending on whether energy to *syn*- CH_3CHOO was provided by methyl-CH vibrational excitation or thermal preparation. Figure 5A shows that VHP concentration from vibEX monotonically increases (blue trace) on the 1 ns time scale and reaches close to 80 % but only for 5 % OH elimination has occurred. Thermal excitation - representative of the initial state of the reactant after ozonolysis of *trans*-2-butene - leads to $\sim 50\%$ population of VHP within 0.3 ns. Over the same time close to 20 % of the trajectories already show OH-elimination. Up to 1 ns more than 30 % of *syn*- CH_3CHOO have completed OH-elimination. Hence, OH production on the 1 ns time scale is about one order of magnitude larger with thermal compared to vibEX preparation of the reactant.

The extended lifetimes of VHP prior to OH elimination can also be rationalized from considering the CCOO dihedral angle ϕ , see Figure 6. Coming from CH_3CHOO the VHP intermediate is formed with a considerable amount of internal energy which is sufficient to

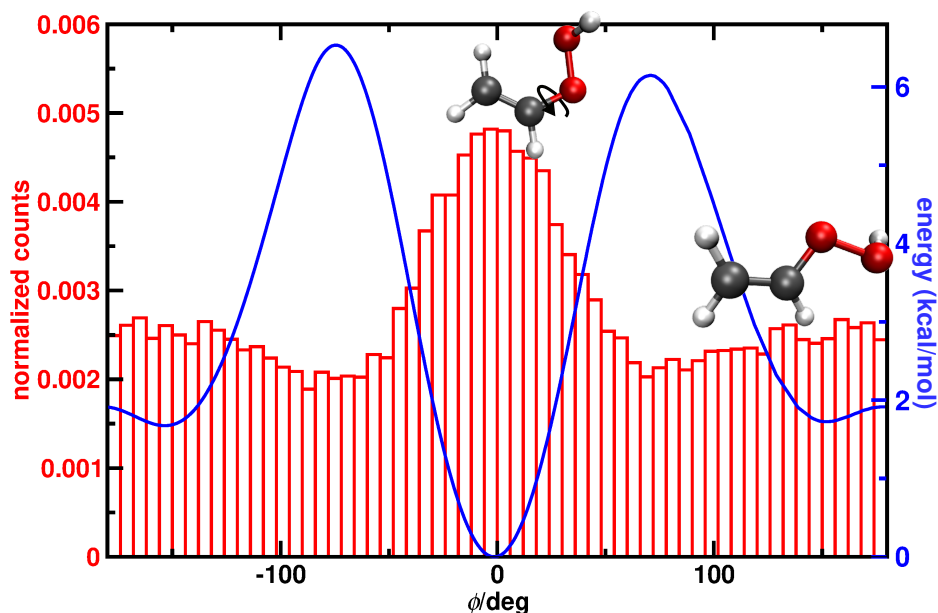


Figure 6: The CCOO dihedral angle distribution $P(\phi)$ for CH_2CHOOH (VHP) from thermal simulations at 902K using ASE. The structure with $\phi = 0^\circ$ corresponds to the -OH group in its *syn* conformation whereas $\phi = \pm 180^\circ$ corresponds to the *anti* conformer. The barrier between 0° and 180° is 6.1 kcal/mol and from 0° to -180° is 6.5 kcal/mol at the MP2/aug-cc-pVTZ level of theory. The histogram of population for the VHP conformation from the simulations is consistent with the PES as *syn*- form is more stable than *anti*- form.

overcome the *syn*/*anti* barrier height of ~ 6 kcal/mol, see also Figure ???. The population distribution $P(\phi)$ for VHP from simulations with PhysNet simulations at 902 K sample all values of ϕ , consistent with the topology of the potential energy curve (blue trace in Figure 6). Analysis of the simulations reveals that OH-elimination occurs from both, *syn*- and *anti*-VHP. This is consistent with the energetic preference for *syn*-VHP but at variance with findings from statistical modeling which reported that all of the VHP decomposes via the *anti*-pathway even if the *syn* form is thermodynamically more stable.²²

Finally, bond length distributions (Figures S8 and S9) show that there is little difference between vibEX and thermal simulations (blue compared with red traces). Thermal distributions from MS-ARMD simulations using only the reactant force field at 300 K (black) are considerably more peaked around the equilibrium values compared with those at 760 K (red). If the 1,4 H-shift reaction is possible (by running the MS-ARMD simulations with

the reactive force field), a few bond length distributions change appreciably (green traces in Figure S8). Excitation of the $C_A H_A$ bond leads to a considerably flatter, more extended distribution, similarly to the $C_B H_D$ distribution. Conversely, the $C_A C_B$ distribution function slightly narrows with an increased peak height at the minimum energy geometry. This suggests that compression of the C-C bond facilitates the 1,4 H-shift reaction.

Discussion and Conclusion

The present work reports on the OH-elimination reaction dynamics of *syn*- CH_3CHOO at thermal and vibrationally induced initial conditions. The thermal process is relevant under conditions that follow the ozonolysis reaction of trans-2-butene which generates a “warm” or “hot” reactant. Vibrational excitation of the methyl-CH-stretch is used in gas-phase laboratory experiments to initiate the reaction. All simulations carried out in the present work find ready 1,4-H-transfer to form the VHP intermediate which then partially reacts to products $CH_2COH+OH$. One of the important “unknowns” remains the dissociation energy D_e^{OO} which would require large-scale multi reference configuration interaction calculations. Of particular note is the finding that tunneling is not required for the entire pathway to obtain rates consistent with experiment.

Because the reaction involves a 1,4 H-shift it is quite likely that tunneling will contribute to the rate. However, it is not the determining factor for reactivity. This differs from earlier efforts based on RRKM theory that reported appreciable rates only when tunneling was included.¹⁸ To further probe this, additional MS-ARMD simulations with $D_e^{OO} = 31.5$ kcal/mol were carried out that with excitation below the barrier. Starting from samples at 300 K with 4000 cm^{-1} of excess energy, OH-elimination occurs on the 2 ns time scale. With the lower, probably preferred, value for D_e^{OO} the reaction is expected to proceed even more

readily.

The PESs used here allow to run a statistically significant number of reactive trajectories on the nanosecond time scale with qualities approaching the MP2 level of theory at the cost of an empirical force field. The two representations have their particular advantages and shortcomings. The MS-ARMD PES has an overall accuracy of ~ 1 kcal/mol which is certainly sufficient for qualitative and semi-quantitative studies. Such a parametrization allows exploration of parameter space as illustrated by the variation of the well depth D_e^{OO} . On the other hand, the PhysNet representation is highly accurate with respect to the reference points. Simulations with this PES are about two orders of magnitude slower which limits broad exploration of initial conditions. One example concerns vibEX simulations with PhysNet. These needed to be carried out with excitation energies ranging from 6500 cm^{-1} to 9000 cm^{-1} in order to observe reactive trajectories due to the O–O dissociation energy of $D_e^{\text{OO}} = 35.7$ kcal/mol. With 9000 cm^{-1} excess energy 1 out of 10 trajectories show OH-elimination on the 1 ns time scale whereas with 8000 cm^{-1} 1 out of 5 trajectories progressed to product on the 5 ns time scale. Excitation with 6500 cm^{-1} does not lead to OH-elimination on the 25 ns time scale. Exploration of the influence of D_e^{OO} within PhysNet is not easily possible without dedicated modification of the underlying data set and training a new NN.

The vibEX simulations indicate that the 1,4 H-shift reaction yields $\sim 80\%$ VHP on the 1 ns time but only 5 % react further to the product, see Figure 5A. Therefore, the second step is a bottleneck for OH generation following vibrational excitation. This is at variance with earlier reports that favour prompt OH-loss and find that the 1,4 H-shift reaction is rate limiting (based on RRKM studies and dynamics initialized at the transition state between *syn*-CH₃CHOO and VHP)^{18,27} but consistent with experimental evidence for significant collisional stabilization of VHP prior to OH formation.^{29,45} One possible explanation for the results found here is rapid IVR after the 1,4 H-shift reaction. This can be seen, e.g., in the

high excitation of the CCOO-dihedral motion after formation of VHP (Figure ??). Similar observations were made for the isomerization of acetaldehyde (AA) to vinylalcohol (VA).³⁵ Excitation of AA with an actinic photon (~ 94 kcal/mol) is not sufficient to trigger isomerization to VA on the 500 ns time scale although the AA \rightarrow VA barrier height is only 68 kcal/mol. Conversely, the thermal simulations which are representative of initial conditions following ozonolysis of trans-2-butene find that on the 1 ns time scale similar amounts of VHP and OH-elimination products are formed with only ~ 20 % of reactant remaining, see Figure 5B. Hence, on this time scale no clear bottleneck can be identified. How much VHP finally reacts to form OH product also depends on the collisional quenching time which is between 1 ns and 10 ns.^{33,46} Hence, if VHP does not form OH product on that time scale it is more likely to lose energy in collisions with the environment which limits OH production from this pathway.

OH-elimination from *syn*-CH₃CHOO following vibrational excitation or thermal preparation yields rates consistent with experiments using full dimensional MS-ARMD and NN-based PESs. The classical MD simulations do not include tunneling effects which are expected to further speed up the first step. Following vibrational excitation of the CI, VHP is found to accumulate. This is different for thermal preparation of *syn*-CH₃CHOO. Overall, the present work provides molecular-level detail for an important reaction in atmospheric chemistry. The approaches used here are generic and expected to be applicable to a range of other reactions.

Data Availability Statement

The PhysNet codes are available at <https://github.com/MMunibas/PhysNet>, and the datasets containing the reference data can be obtained from from github <https://github.com/MMunibas/Criegee.git>.

Acknowledgments

This work was supported by the Swiss National Science Foundation through grants 200021-117810, 200020-188724 and the NCCR MUST, and the University of Basel.

Supporting information

The supplementary material contains the methods, tables with the number of reactive trajectories, and figures for rate calculations, lifetime statistics, and coordinate distributions functions.

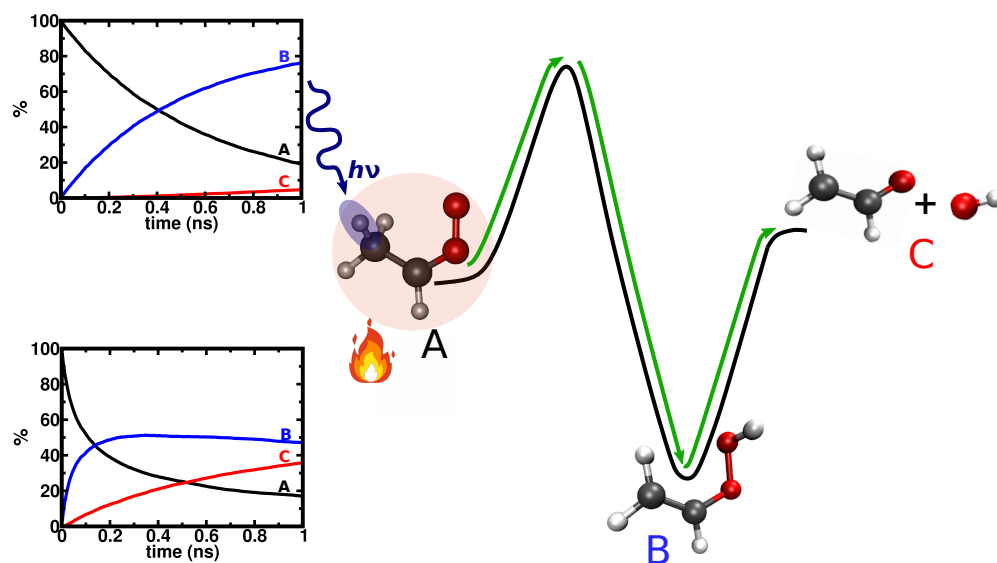


Figure 7: Table of Contents graphics: Depending on the initial preparation the decomposition dynamics of *syn*-CH₃CHOO differs.

References

- (1) Stone, D.; Whalley, L. K.; Heard, D. E. Tropospheric OH and HO₂ radicals: field measurements and model comparisons. *Chem. Soc. Rev.* **2012**, *41*, 6348–6404.

- (2) Gligorovski, S.; Strekowski, R.; Barbati, S.; Vione, D. Environmental implications of hydroxyl radicals (OH). *Chem. Rev.* **2015**, *115*, 13051–13092.
- (3) Levy, H. Normal atmosphere: Large radical and formaldehyde concentrations predicted. *Science* **1971**, *173*, 141–143.
- (4) Emmerson, K.; Carslaw, N. Night-time radical chemistry during the TORCH campaign. *Atmos. Environ.* **2009**, *43*, 3220–3226.
- (5) Khan, M.; Percival, C.; Caravan, R.; Taatjes, C.; Shallcross, D. Criegee intermediates and their impacts on the troposphere. *Environ. Sci.: Process. Impacts* **2018**, *20*, 437–453.
- (6) Criegee, R.; Wenner, G. Die Ozonisierung des 9, 10-Oktalins. *Justus Liebigs Ann. Chem.* **1949**, *564*, 9–15.
- (7) Alam, M. S.; Camredon, M.; Rickard, A. R.; Carr, T.; Wyche, K. P.; Hornsby, K. E.; Monks, P. S.; Bloss, W. J. Total radical yields from tropospheric ethene ozonolysis. *Phys. Chem. Chem. Phys.* **2011**, *13*, 11002–11015.
- (8) Novelli, A.; Vereecken, L.; Lelieveld, J.; Harder, H. Direct observation of OH formation from stabilised Criegee intermediates. *Phys. Chem. Chem. Phys.* **2014**, *16*, 19941–19951.
- (9) Taatjes, C. A. Criegee intermediates: What direct production and detection can teach us about reactions of carbonyl oxides. *Ann. Rev. Phys. Chem.* **2017**, *68*, 183–207.
- (10) Mauldin Iii, R.; Berndt, T.; Sipilä, M.; Paasonen, P.; Petäjä, T.; Kim, S.; Kurtén, T.; Stratmann, F.; Kerminen, V.-M.; Kulmala, M. A new atmospherically relevant oxidant of sulphur dioxide. *Nature* **2012**, *488*, 193–196.

- (11) Atkinson, R.; Aschmann, S. M. Hydroxyl radical production from the gas-phase reactions of ozone with a series of alkenes under atmospheric conditions. *Environ. Sci. Technol.* **1993**, *27*, 1357–1363.
- (12) Kuwata, K. T.; Hermes, M. R.; Carlson, M. J.; Zogg, C. K. Computational studies of the isomerization and hydration reactions of acetaldehyde oxide and methyl vinyl carbonyl oxide. *J. Phys. Chem. A* **2010**, *114*, 9192–9204.
- (13) Liu, F.; Beames, J. M.; Petit, A. S.; McCoy, A. B.; Lester, M. I. Infrared-driven unimolecular reaction of CH₃CHOO Criegee intermediates to OH radical products. *Science* **2014**, *345*, 1596–1598.
- (14) Vereecken, L.; Novelli, A.; Taraborrelli, D. Unimolecular decay strongly limits the atmospheric impact of Criegee intermediates. *Phys. Chem. Chem. Phys.* **2017**, *19*, 31599–31612.
- (15) Gutbrod, R.; Kraka, E.; Schindler, R. N.; Cremer, D. Kinetic and theoretical investigation of the gas-phase ozonolysis of isoprene: Carbonyl oxides as an important source for OH radicals in the atmosphere. *J. Am. Chem. Soc.* **1997**, *119*, 7330–7342.
- (16) Long, B.; Bao, J. L.; Truhlar, D. G. Atmospheric chemistry of Criegee intermediates: Unimolecular reactions and reactions with water. *J. Am. Chem. Soc.* **2016**, *138*, 14409–14422.
- (17) Yin, C.; Takahashi, K. How does substitution affect the unimolecular reaction rates of Criegee intermediates? *Phys. Chem. Chem. Phys.* **2017**, *19*, 12075–12084.
- (18) Fang, Y.; Liu, F.; Barber, V. P.; Klippenstein, S. J.; McCoy, A. B.; Lester, M. I. Communication: Real time observation of unimolecular decay of Criegee intermediates to OH radical products. *J. Chem. Phys.* **2016**, *144*.

- (19) Fang, Y.; Liu, F.; Barber, V. P.; Klippenstein, S. J.; McCoy, A. B.; Lester, M. I. Deep tunneling in the unimolecular decay of CH₃CHOO Criegee intermediates to OH radical products. *J. Chem. Phys.* **2016**, *145*, 234308.
- (20) Baer, T.; Hase, W. L. *Unimolecular reaction dynamics: theory and experiments*; Oxford University Press, 1996.
- (21) Green, A. M.; Barber, V. P.; Fang, Y.; Klippenstein, S. J.; Lester, M. I. Selective deuteration illuminates the importance of tunneling in the unimolecular decay of Criegee intermediates to hydroxyl radical products. *Proc. Natl. Acad. Sci. USA* **2017**, *114*, 12372–12377.
- (22) Kuwata, K. T.; Luu, L.; Weberg, A. B.; Huang, K.; Parsons, A. J.; Peebles, L. A.; Rackstraw, N. B.; Kim, M. J. Quantum chemical and statistical rate theory studies of the vinyl hydroperoxides formed in trans-2-butene and 2, 3-dimethyl-2-butene ozonolysis. *J. Phys. Chem. A* **2018**, *122*, 2485–2502.
- (23) Wang, X.; Bowman, J. M. Two Pathways for Dissociation of Highly Energized syn-CH₃CHOO to OH Plus Vinyloxy. *J. Phys. Chem. Lett.* **2016**, *7*, 3359–3364.
- (24) Nguyen, T. L.; McCaslin, L.; McCarthy, M. C.; Stanton, J. F. Communication: Thermal unimolecular decomposition of syn-CH₃CHOO: A kinetic study. 2016.
- (25) Zhou, X.; Liu, Y.; Dong, W.; Yang, X. Unimolecular reaction rate measurement of syn-CH₃CHOO. *J. Phys. Chem. Lett.* **2019**, *10*, 4817–4821.
- (26) Kurten, T.; Donahue, N. M. MRCISD studies of the dissociation of vinylhydroperoxide, CH₂CHOOH: There is a saddle point. *J. Phys. Chem. A* **2012**, *116*, 6823–6830.
- (27) Kidwell, N. M.; Li, H.; Wang, X.; Bowman, J. M.; Lester, M. I. Unimolecular dissociation dynamics of vibrationally activated CH₃CHOO Criegee intermediates to OH radical products. *Nat. Chem.* **2016**, *8*, 509–514.

- (28) Johnson, D.; Marston, G. The gas-phase ozonolysis of unsaturated volatile organic compounds in the troposphere. *Chem. Soc. Rev.* **2008**, *37*, 699–716.
- (29) Donahue, N. M.; Drozd, G. T.; Epstein, S. A.; Presto, A. A.; Kroll, J. H. Adventures in ozoneland: down the rabbit-hole. *Phys. Chem. Chem. Phys.* **2011**, *13*, 10848–10857.
- (30) Brooks, B. R.; Brooks III, C. L.; Mackerell Jr, A. D.; Nilsson, L.; Petrella, R. J.; Roux, B.; Won, Y.; Archontis, G.; Bartels, C.; Boresch, S. et al. CHARMM: the biomolecular simulation program. *J. Comput. Chem.* **2009**, *30*, 1545–1614.
- (31) Larsen, A. H.; Mortensen, J. J.; Blomqvist, J.; Castelli, I. E.; Christensen, R.; Dulak, M.; Friis, J.; Groves, M. N.; Hammer, B.; Hargus, C. et al. The atomic simulation environment – a Python library for working with atoms. *J. Phys. Condens. Matter* **2017**, *29*, 273002.
- (32) Tong, X.; Nagy, T.; Reyes, J. Y.; Germann, M.; Meuwly, M.; Willitsch, S. State-selected ion-molecule reactions with Coulomb-crystallized molecular ions in traps. *Chem. Phys. Lett.* **2012**, *547*, 1–8.
- (33) Yosa Reyes, J.; Nagy, T.; Meuwly, M. Competitive reaction pathways in vibrationally induced photodissociation of H₂SO₄. *Phys. Chem. Chem. Phys.* **2014**, *16*, 18533–18544.
- (34) Sweeny, B. C.; Pan, H.; Kassem, A.; Sawyer, J. C.; Ard, S. G.; Shuman, N. S.; Viggiano, A. A.; Brickel, S.; Unke, O. T.; Upadhyay, M. et al. Thermal activation of methane by MgO⁺: temperature dependent kinetics, reactive molecular dynamics simulations and statistical modeling. *Phys. Chem. Chem. Phys.* **2020**, *22*, 8913–8923.
- (35) Käser, S.; Unke, O. T.; Meuwly, M. Isomerization and decomposition reactions of acetaldehyde relevant to atmospheric processes from dynamics simulations on neural network-based potential energy surfaces. *J. Chem. Phys.* **2020**, *152*, 214304.

- (36) Käser, S.; Unke, O. T.; Meuwly, M. Reactive dynamics and spectroscopy of hydrogen transfer from neural network-based reactive potential energy surfaces. *New J. Phys.* **2020**, *22*, 055002.
- (37) Rivero, U.; Unke, O. T.; Meuwly, M.; Willitsch, S. Reactive atomistic simulations of Diels-Alder reactions: The importance of molecular rotations. *J. Chem. Phys.* **2019**, *151*, 104301.
- (38) Yosa Reyes, J.; Brickel, S.; Unke, O. T.; Meuwly, M. HSO₃Cl : a prototype molecule for studying OH-stretching overtone induced photodissociation. *Phys. Chem. Chem. Phys.* **2016**, *18*, 6780–6788.
- (39) Boltachev, G. S.; Schmelzer, J. W. On the definition of temperature and its fluctuations in small systems. *J. Chem. Phys.* **2010**, *133*, 134509.
- (40) Soloviov, M.; Das, A. K.; Meuwly, M. Structural Interpretation of Metastable States in Myoglobin–NO. *Angew. Chem. Int. Ed.* **2016**, *55*, 10126–10130.
- (41) Kroll, J. H.; Clarke, J. S.; Donahue, N. M.; Anderson, J. G. Mechanism of HO_x formation in the gas-phase ozone- alkene reaction. 1. Direct, pressure-dependent measurements of prompt OH yields. *J. Phys. Chem. A* **2001**, *105*, 1554–1560.
- (42) Osborn, D. L.; Taatjes, C. A. The physical chemistry of Criegee intermediates in the gas phase. *Intern. Rev. Phys. Chem.* **2015**, *34*, 309–360.
- (43) Wang, Z.; Dyakov, Y. A.; Bu, Y. Dynamics Insight into Isomerization and Dissociation of Hot Criegee Intermediate CH₃CHOO. *J. Phys. Chem. A* **2019**, *123*, 1085–1090.
- (44) Kalinowski, J.; Räsänen, M.; Heinonen, P.; Kilpeläinen, I.; Gerber, R. B. Isomerization and decomposition of a Criegee intermediate in the ozonolysis of alkenes: dynamics using a multireference potential. *Angew. Chem. Int. Ed.* **2014**, *126*, 269–272.

- (45) Drozd, G. T.; Kroll, J.; Donahue, N. M. 2, 3-Dimethyl-2-butene (TME) ozonolysis: pressure dependence of stabilized Criegee intermediates and evidence of stabilized vinyl hydroperoxides. *J. Phys. Chem. A* **2011**, *115*, 161–166.
- (46) Drozd, G. T.; Kurtén, T.; Donahue, N. M.; Lester, M. I. Unimolecular decay of the dimethyl-substituted Criegee intermediate in alkene ozonolysis: Decay time scales and the importance of tunneling. *J. Phys. Chem. A* **2017**, *121*, 6036–6045.

Supplementary Information:

Meenu Upadhyay and Markus Meuwly

*Department of Chemistry, University of Basel, Klingelbergstrasse 80 , CH-4056 Basel,
Switzerland.*

E-mail:

Computational Methods

This section presents the different computational methods employed. Two different representations for the intermolecular interactions are used. One is a multi-state reactive force field (MS-ARMD), and the second one is a machine learning-based representation using PhysNet. Finally, the molecular dynamics (MD) simulations are also described.

Reactive Force Fields

MS-ARMD is a computationally efficient, energy-conserving surface crossing algorithm to investigate chemical reactions based on empirical force fields.¹ It uses parameterized force fields for the reactant and product state and GAPOs (GAussian×POLynomials) to describe the surface crossing region, i.e. the region around the transition state (TS). The parametrized force fields for the reactant and product complexes are iteratively fit to reference data from electronic structure calculations.

In the present work, two representations of the full-dimensional, reactive PES were developed based on two quantum chemical treatments. They included MS-ARMD and PhysNet for the

representation and the MP2/6-311++G(2d,2p) and MP2/aug-cc-pVTZ levels of theory for the reference calculations which were carried out using Gaussian09² and MOLPRO.³ This allows validation of the representations and direct assessment of the level of theory.

The initial parameters for the reactant (*syn*-CH₃CHOO, methyl-substituted Criegee intermediate) and product (CH₂CHOOH, vinyl hydroperoxide) were taken from SwissParam.⁴ First, representative structures for CH₃CHOO (1612) and CH₂CHOOH (1650) were sampled from 500 ps MD simulations at 300 K. For these structures, energies were determined at the MP2/6-311++G(2d,2p) level of theory. These were fit separately to parametrized force fields for the reactant and the product using a downhill simplex⁵ algorithm. Parametrization starts with a set of 100 structures for CH₃CHOO and CH₂CHOOH and first fitting for the two states were carried out which was then followed by further MD simulations using this improved set of parameters from which another 200 structures was extracted and included in the fit. Several rounds of refinements were done until the root mean squared deviation for the final set between the target (*ab initio*) and the fitted energies for CH₃CHOO and CH₂CHOOH reached 1.1 kcal/mol and 1.2 kcal/mol, respectively. The bonds involved in bond breaking and bond formation (the three C-H, the O-O, and the O-H bonds) were described by Morse potentials and the charges from *ab initio* calculations at the MP2/6-311++G(2d,2p) level of theory. Generalized Lennard-Jones potential is included and fitted, to represent the van der Waals interaction between atoms (between H_A and O_B in reactant FF and between H_A and C_A in product FF) in the reactive region.

The reactant and product force fields are connected by using GAPO-functions to yield a continuous connection along the reaction path. For this, the intrinsic reaction coordinate (IRC) between reactant and product was also determined and included in the fitting. To parametrize the adiabatic barrier, genetic algorithm was used to parametrize the Gaussian×Polynomial (GAPO)¹ functions and to reproduce the energies along the reaction path.

The TS barrier for *syn*-CH₃CHOO is 16.02 kcal/mol.

Neural Network

As an alternative to MS-ARMD a NN-based reactive force field was trained based on the PhysNet architecture,⁶ which is designed to construct PES after learning molecular properties like energy, forces, charges and dipole moments from ab initio reference data. Here, MP2/aug-cc-pVTZ level of theory⁷ is used for generation of ab initio reference data and the energies, forces and dipole moments are calculated using MOLPRO software package.

Following the “amons” approach,⁸ a set of molecules (Figure S1) are included covering a range of fragmentation reactant, products, stable intermediates and van der Waals complexes in the dataset. To obtain a broad range of molecular geometries, MD simulations were started from optimized geometries which are propagated using Langevin dynamics at 1000 K with a time step of 0.1 fs. Then, the data set is extended based on adaptive sampling and normal mode sampling.⁹ The final dataset used for training contains 105403 structures, which was then split into training (84322), validation (10540) and test set (10541). The TS barrier for *syn*-CH₃CHOO is 14.9 kcal/mol.

Molecular Dynamics Simulations

The MD simulations for MS-ARMD were carried out with a suitably modified version of CHARMM.¹⁰ Simulations based on PhysNet were run with the Atom Simulation Environment (ASE).¹¹

For the thermal simulations based on MS-ARMD the geometry optimized structure of CH₃CHOO was heated to the desired temperature and equilibrated for 50 ps with a time

step of 0.1 fs, followed by the 100 ps / 1 ns of free dynamics. The simulations with ASE were initialized from the optimized structures. Then, momenta were assigned from a Maxwell-Boltzmann distribution at the desired temperature which is then followed by Langevin dynamics for 100 ps with $\Delta t = 0.1$ fs.

The vibrationally excited (vibEX) simulations also started from a geometry optimized structure of CH₃CHOO. Then, the system is heated to 300 K and equilibrated for 50 ps with a time step of $\Delta t = 0.1$ fs, followed by 1 ns of free dynamics. From this simulation, coordinates and velocities were saved regularly to obtain 70000 initial conditions for each of the excitation energies. Then a non-equilibrium state is prepared by scaling the instantaneous velocity vector along the OH mode. 10000 independent trajectories for each excitation energies were run with a simulation time of 1 ns for $D_e^{\text{OO}} = 31.5$ kcal/mol and 100 ps for $D_e^{\text{OO}} = 23.5$ kcal/mol. For the vibEX simulations with ASE, the momenta were assigned from a Maxwell-Boltzmann distribution at 300 K to the geometry optimized structure of CH₃CHOO, followed by 50 ps of free dynamics with $\Delta t = 0.1$ fs. Then a non-equilibrium state is prepared by scaling the instantaneous velocity vector along the CH mode. 10000 independent trajectories were run for each excitation energy for 100 ps with $\Delta t = 0.1$ fs.

In addition to the explicit MD simulations, the minimum energy path was also determined.¹² This path connecting reactant and product geometry, passing through the exact transition state with zero excess energy was calculated by assigning momenta along the normal mode vector. Then, the MD simulation from transition state to both reactant and product channel using the PhysNet PES.

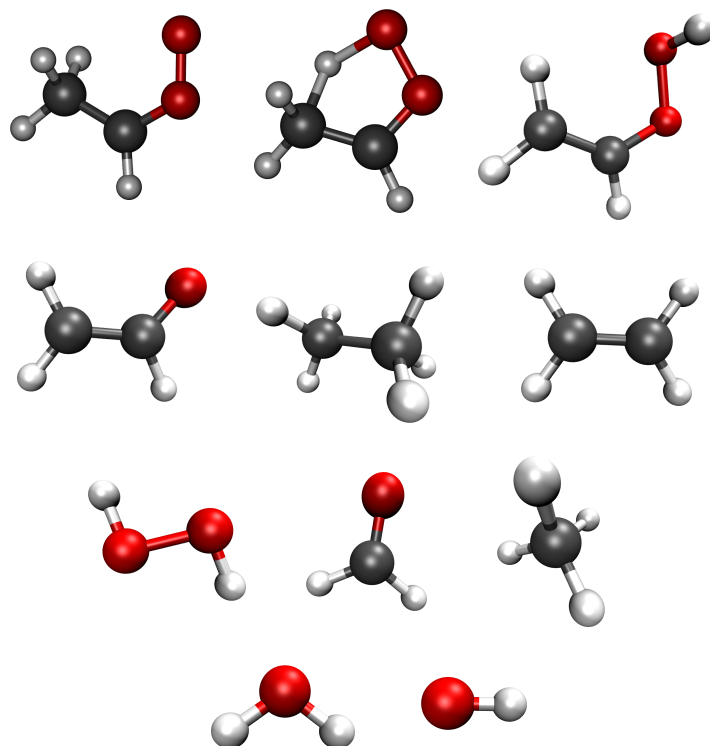


Figure S1: Different structures and atoms⁸ used for training the neural network representation. The first row contains the reactant, transition, product structures and subsequent rows contain their fragmented structures.

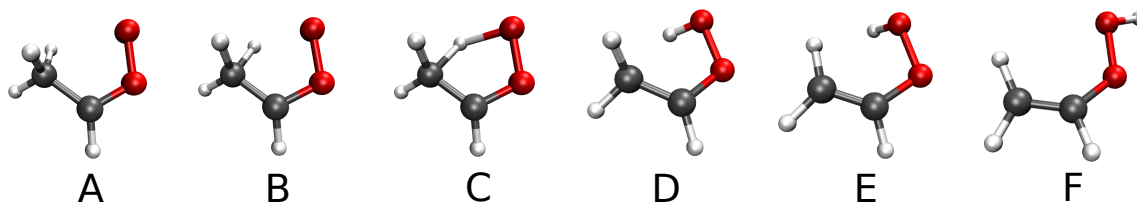


Figure S2: Minimum Dynamic Path¹² on the PhysNet PES for the 1,4 Hydrogen shift from carbon to oxygen in Criegee intermediates. The reaction proceeds through a five membered transition state for which $r_{\text{CH}} = 1.30 \text{ \AA}$ and $r_{\text{OH}} = 1.41 \text{ \AA}$. From A \rightarrow F the C-C distance change is reported in Figure S5. The C-O distance changes from 1.27 \AA to 1.37 \AA and the O-O distance changes from 1.32 \AA to 1.45 \AA .

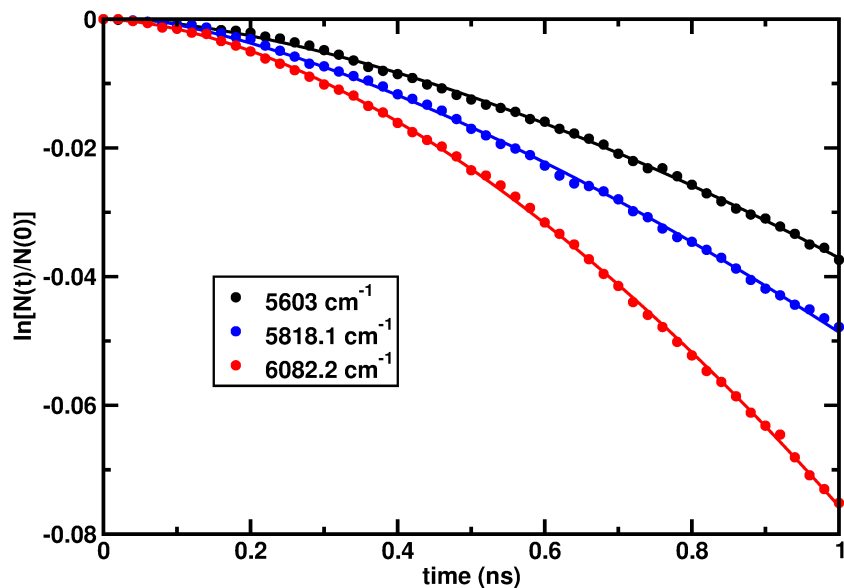


Figure S3: Fit of $\ln[N(t)/N(0)]$ for $D_e = 31.5$ kcal/mol from vibEX simulations at energies of 5603 cm^{-1} , 5818.1 cm^{-1} and 6082.2 cm^{-1} to a stretched exponential decay.

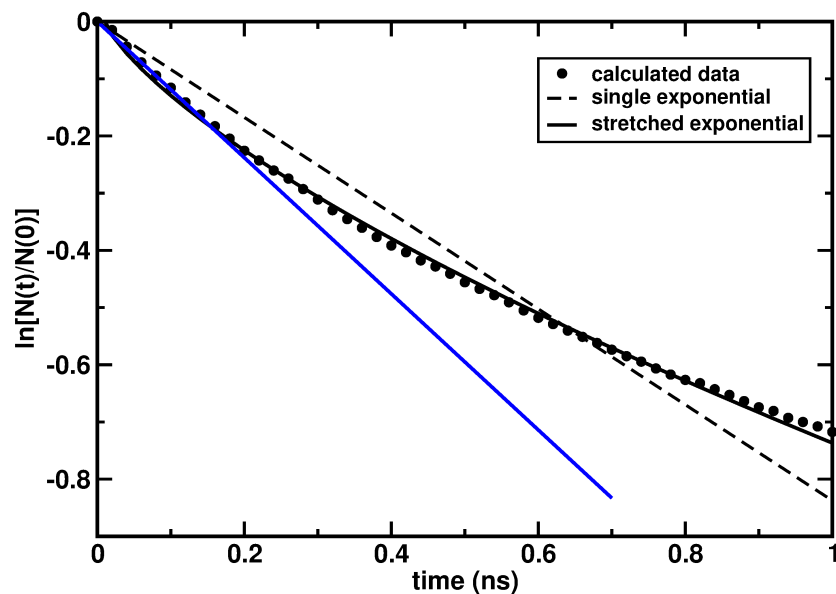


Figure S4: Fit of $\ln[N(t)/N(0)]$ for $D_e = 31.5$ kcal/mol from thermal simulations at 956 K where blue solid line is to show that till 200 ps the data follows a linear fit.

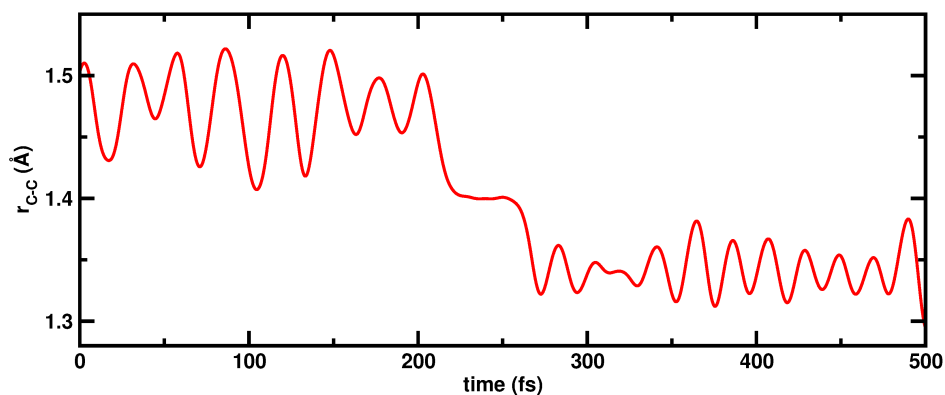


Figure S5: C-C distance along the minimum dynamic path as a function of time from CH_3CHOO to CH_2CHOOH .

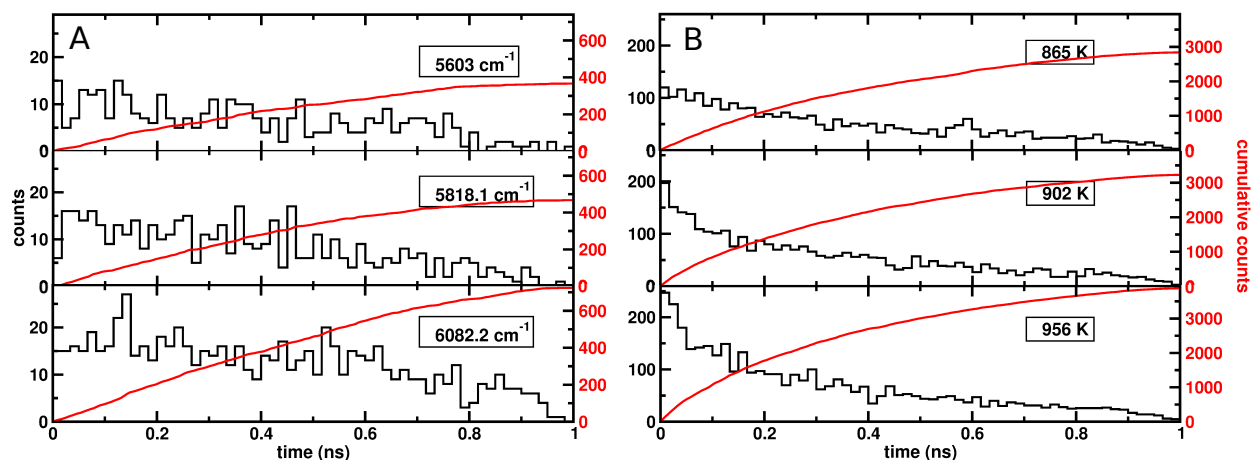


Figure S6: Distribution of vinyl hydroperoxide lifetimes before OH formation from vibEX (panel A) and thermal (panel B) using MS-ARMD and $D_e^{\text{OO}} = 31.5$ kcal/mol. Histograms (black) and cumulative (red line) events are reported in the same panel with corresponding labels along the y -axes. Note the different scaling of the y -axes in panels A and B. The kinetic temperatures used to label the thermal simulations (panel B) are close to the excitation energies used in the vibEX simulations (panel A).

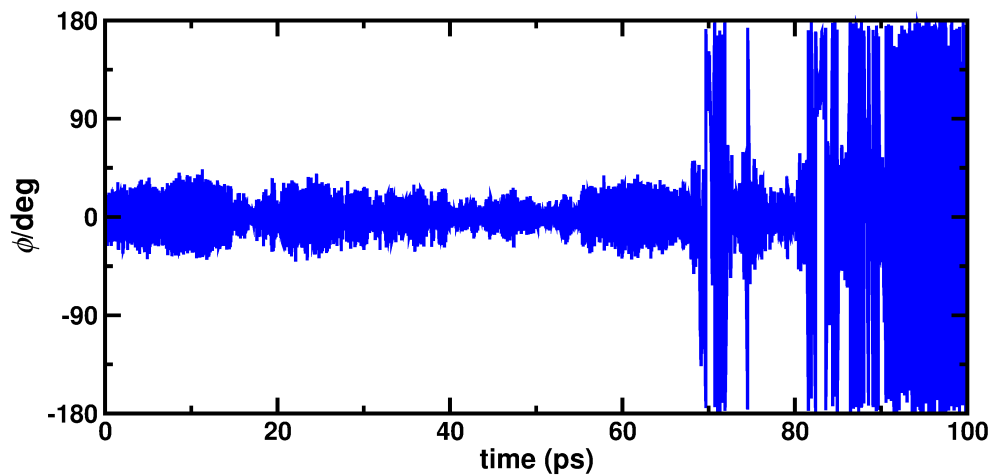


Figure S7: Time series $\phi(t)$ from a thermal trajectory at 902 K using ASE. Until $t = 67$ ps the system is in the *syn*-CH₃CHO state with $\phi \sim 0$. Between $t = 67$ and 90 ps it is in VHP. Here, $\phi \in [-180.. +180]$, but most time is spent in the *syn*-form $\phi \in [-60.. +60]$. At $t = 90$ ps OH dissociation takes place and ϕ loses its meaning.

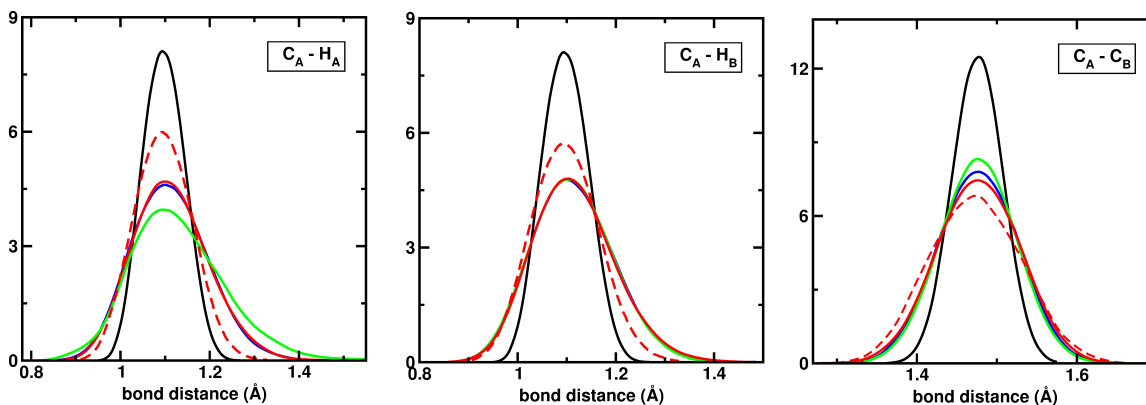


Figure S8: Bond distance distributions of $C_A H_A$, $C_A H_B$ and $C_A C_B$ for *syn*-CH₃CHO at 300 K (black) 250 ps, vibEX at 5983 cm⁻¹ from 250 ps long simulation (blue) using the reactant FF, thermal simulations at 760 K from 250 ps long simulation (red) using the reactant FF and vibEX at 5983 cm⁻¹ from reactive simulation showing H-transfer within 10 ps (green) using MS-ARMD. Bond distance distribution from thermal simulations (red dashed) at 932 K using ASE.

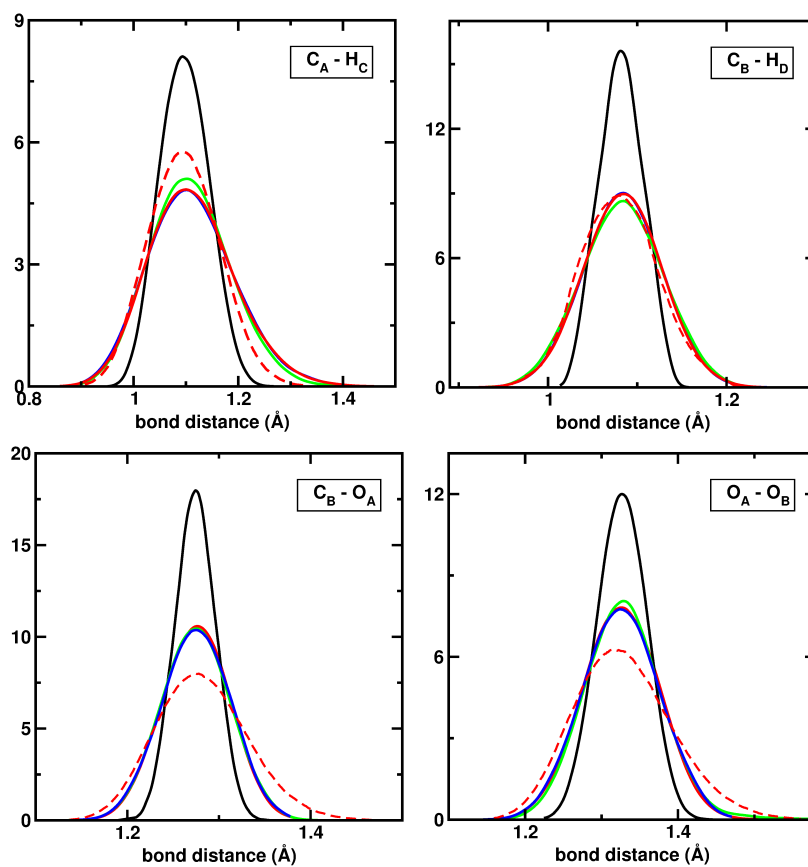


Figure S9: Bond distance distribution for *syn*-CH₃CHOO at 300 K (black solid line), Vibrationally activated at 5983 cm⁻¹ from 250 ps long simulation (blue solid line) using reactant FF, thermally activated at 760 K from 250 ps long simulation (red solid line) using reactant FF and Vibrationally activated at 5983 cm⁻¹ from reactive simulation showing H-transfer in 10 ps (green solid line) using MS-ARMD. Bond distance distribution from thermal simulations (red dashed) at 932 K using ASE.

Table S1: Total number of H- transfer and OH-elimination reactions from MS-ARMD vibEX simulations with $D_e^{\text{OO}} = 31.5$ kcal/mol. The total simulation time is 1 ns for each trajectory and 10000 independent simulations are carried out. The aggregated number of reactions up to time t is reported.

IR excitation(cm^{-1})	t (ns)	H transfer	OH formed	IR excitation(cm^{-1})	t (ns)	H transfer	OH formed
5603	0.1	1307	8	5950.9	0.1	1860	12
	0.2	2479	21		0.2	3286	42
	0.3	3498	48		0.3	4484	83
	0.4	4378	85		0.4	5447	147
	0.5	5104	124		0.5	6272	209
	0.6	5679	158		0.6	6874	267
	0.7	6212	207		0.7	7344	342
	0.8	6700	254		0.8	7763	422
	0.9	7120	305		0.9	8089	506
	1.0	7452	367		1.0	8413	605
5709	0.1	1462	8	5983.5	0.1	1873	15
	0.2	2641	24		0.2	3371	50
	0.3	3709	49		0.3	4551	98
	0.4	4568	81		0.4	5487	161
	0.5	5325	134		0.5	6255	226
	0.6	5938	188		0.6	6932	307
	0.7	6474	253		0.7	7440	388
	0.8	6953	316		0.8	7896	460
	0.9	7346	376		0.9	8228	555
	1.0	7712	431		1.0	8528	647
5747.6	0.1	1544	10	6082.2	0.1	2128	15
	0.2	2761	35		0.2	3664	50
	0.3	3786	71		0.3	4825	101
	0.4	4761	109		0.4	5853	160
	0.5	5510	154		0.5	6661	232
	0.6	6200	208		0.6	7295	311
	0.7	6697	264		0.7	7788	406
	0.8	7142	334		0.8	8225	509
	0.9	7526	401		0.9	8547	612
	1.0	7873	485		1.0	8774	724
5818.1	0.1	1695	9				
	0.2	2996	31				
	0.3	4119	73				
	0.4	4999	116				
	0.5	5782	169				
	0.6	6415	225				
	0.7	6943	276				
	0.8	7381	340				
	0.9	7747	410				
	1.0	8097	467				

Table S2: Total number of H- transfer and OH-elimination reactions from MS-ARMD vibEX simulations with $D_e^{\text{OO}} = 23.5$ kcal/mol. The total simulation time is 100 ps for each trajectory and 10000 independent simulations are carried out. The aggregated number of reactions up to time t is reported.

IR excitation(cm^{-1})	t (ns)	H transfer	OH formed	IR excitation(cm^{-1})	t (ns)	H transfer	OH formed
5603	10	242	2	5950.9	10	267	3
	20	396	7		20	460	17
	30	534	16		30	644	27
	40	674	28		40	829	52
	50	795	50		50	1043	74
	60	935	68		60	1242	105
	70	1084	101		70	1409	133
	80	1215	128		80	1579	174
	90	1327	153		90	1749	215
	100	1440	178		100	1927	257
5709	10	215	3	5983.5	10	311	5
	20	361	12		20	513	23
	30	512	19		30	706	37
	40	655	27		40	881	58
	50	814	54		50	1053	84
	60	942	74		60	1264	118
	70	1090	90		70	1440	154
	80	1232	116		80	1599	181
	90	1351	144		90	1803	227
	100	1467	178		100	1956	275
5747.6	10	238	3	6082.2	10	337	4
	20	409	11		20	556	18
	30	585	21		30	766	38
	40	753	41		40	978	67
	50	912	62		50	1195	108
	60	1060	90		60	1414	140
	70	1187	110		70	1628	182
	80	1328	145		80	1816	226
	90	1458	178		90	1990	288
	100	1578	212		100	2176	344
5818.1	10	262	3				
	20	450	12				
	30	607	28				
	40	791	48				
	50	946	68				
	60	1104	95				
	70	1244	132				
	80	1390	172				
	90	1562	218				
	100	1711	253				

Table S3: Total number of H- transfer and OH-elimination reactions from MS-ARMD thermal simulations with $D_e^{\text{OO}} = 31.5$ kcal/mol. The total simulation time is 1 ns for each trajectory and 10000 independent simulations are carried out. The aggregated number of reactions up to time t is reported. Some simulations shown H-transfer in heating step which are excluded from the total.

T (K)	Total	t (ns)	H transfer	OH formed	T (K)	Total	t (ns)	H transfer	OH formed
865	9292	0.1	4034	416	925	8894	0.1	4648	657
		0.2	5272	861			0.2	5816	1230
		0.3	5905	1236			0.3	6395	1668
		0.4	6328	1561			0.4	6764	2094
		0.5	6642	1831			0.5	7006	2414
		0.6	6858	2076			0.6	7193	2685
		0.7	7039	2295			0.7	7337	2897
		0.8	7172	2501			0.8	7466	3117
		0.9	7268	2680			0.9	7551	3294
		1.0	7377	2839			1.0	7621	3449
877	9227	0.1	4228	510	932	8848	0.1	4663	690
		0.2	5351	971			0.2	5777	1311
		0.3	5959	1336			0.3	6358	1798
		0.4	6356	1684			0.4	6687	2178
		0.5	6640	1953			0.5	6960	2472
		0.6	6875	2181			0.6	7138	2746
		0.7	7048	2442			0.7	7305	2983
		0.8	7184	2610			0.8	7406	3165
		0.9	7308	2771			0.9	7520	3364
		1.0	7419	2924			1.0	7590	3525
886	9165	0.1	4269	490	956	8789	0.1	4982	827
		0.2	5415	974			0.2	6076	1532
		0.3	6054	1374			0.3	6620	2026
		0.4	6428	1717			0.4	6948	2455
		0.5	6708	1981			0.5	7152	2774
		0.6	6922	2273			0.6	7319	3063
		0.7	7069	2477			0.7	7435	3308
		0.8	7207	2701			0.8	7535	3528
		0.9	7339	2871			0.9	7621	3717
		1.0	7449	3039			1.0	7683	3880
902	9032	0.1	4347	601					
		0.2	5514	1115					
		0.3	6123	1539					
		0.4	6503	1895					
		0.5	6748	2191					
		0.6	6993	2454					
		0.7	7179	2684					
		0.8	7307	2876					
		0.9	7392	3068					
		1.0	7493	3228					

Table S4: Total number of H- transfer and OH-elimination reactions from MS-ARMD thermal simulations with $D_e^{\text{OO}} = 23.5$ kcal/mol. The total simulation time is 100 ps for each trajectory and 10000 independent simulations are carried out. The aggregated number of reactions up to time t is reported. Some simulations shown H-transfer in heating step which are excluded from the total.

T (K)	Total	t (ns)	H transfer	OH formed	T (K)	Total	t (ns)	H transfer	OH formed
865	9338	10	827	93	925	9000	10	1239	204
		20	1496	286			20	2103	542
		30	2022	524			30	2682	905
		40	2426	768			40	3143	1249
		50	2765	998			50	3538	1533
		60	3081	1224			60	3846	1818
		70	3332	1440			70	4139	2095
		80	3554	1631			80	4370	2342
		90	3767	1827			90	4574	2555
		100	3970	2023			100	4752	2768
877	9324	10	954	146	932	9000	10	1231	170
		20	1651	385			20	2112	472
		30	2196	615			30	2721	835
		40	2604	860			40	3203	1196
		50	2989	1107			50	3599	1525
		60	3279	1352			60	3911	1823
		70	3560	1575			70	4167	2100
		80	3787	1788			80	4396	2349
		90	4016	1973			90	4563	2550
		100	4188	2173			100	4750	2770
886	9257	1037	34	133	956	8917	10	1356	216
		20	1768	401			20	2268	616
		30	2283	650			30	2899	997
		40	2698	922			40	3382	1357
		50	3103	1174			50	3753	1695
		60	3411	1406			60	4085	2011
		70	3687	1642			70	4373	2277
		80	3900	1850			80	4623	2560
		90	4130	2066			90	4794	2795
		100	4332	2258			100	4989	3014
902	9167	10	1065	148					
		20	1822	410					
		30	2427	681					
		40	2876	986					
		50	3277	1232					
		60	3601	1520					
		70	3881	1766					
		80	4113	2001					
		90	4334	2232					
		100	4538	2407					

Table S5: Total number of H- transfer and OH-elimination reactions from PhysNet thermal simulations. The total simulation time is 100 ps for each trajectory and 10000 independent simulations are carried out. The aggregated number of reactions up to time t is reported. Some simulations shown H-transfer in heating step which are excluded from the total.

T (K)	Total	t (ns)	H transfer	OH formed	T (K)	Total	t (ns)	H transfer	OH formed
865	9980	10	15	12	902	9891	10	30	24
		20	35	29			20	48	43
		30	44	43			30	68	62
		40	56	54			40	90	84
		50	69	66			50	108	103
		60	78	73			60	121	116
		70	90	88			70	134	131
		80	99	98			80	144	143
		90	107	106			90	161	153
		100	112	110			100	171	169
877	9978	10	24	19	925	9970	10	40	30
		20	38	34			20	58	53
		30	51	48			30	75	70
		40	62	62			40	100	92
		50	74	74			50	117	113
		60	90	83			60	141	136
		70	102	97			70	165	159
		80	120	114			80	175	172
		90	131	130			90	195	188
		100	141	139			100	211	208
886	9956	10	26	21	956	9961	10	41	34
		20	48	42			20	77	69
		30	62	55			30	108	102
		40	85	75			40	144	133
		50	99	98			50	164	162
		60	112	110			60	192	180
		70	126	125			70	208	207
		80	143	139			80	227	225
		90	153	149			90	242	239
		100	164	162			100	260	260

References

- (1) Nagy, T.; Yosa Reyes, J.; Meuwly, M. Multisurface Adiabatic Reactive Molecular Dynamics. *J. Chem. Theory Comput.* **2014**, *10*, 1366–1375.
- (2) Gaussian09, R. A. 1, mj frisch, gw trucks, hb schlegel, ge scuseria, ma robb, jr cheeseman, g. Scalmani, v. Barone, b. Mennucci, ga petersson et al., gaussian. *Inc., Wallingford CT* **2009**, *121*, 150–166.
- (3) Werner, H.-J. et al. The Molpro quantum chemistry package. *J. Chem. Phys.* **2020**, *152*, 144107.
- (4) Zoete, V.; Cuendet, M. A.; Grosdidier, A.; Michielin, O. SwissParam: a fast force field generation tool for small organic molecules. *J. Comput. Chem.* **2011**, *32*, 2359–2368.
- (5) Nelder, J. A.; Mead, R. A simplex method for function minimization. *Comput. J.* **1965**, *7*, 308–313.
- (6) Unke, O. T.; Meuwly, M. PhysNet: A neural network for predicting energies, forces, dipole moments, and partial charges. *J. Chem. Theory Comput.* **2019**, *15*, 3678–3693.
- (7) Møller, C.; Plesset, M. S. Note on an approximation treatment for many-electron systems. *Phys. Rev.* **1934**, *46*, 618.
- (8) Huang, B.; von Lilienfeld, O. A. Quantum machine learning using atom-in-molecule-based fragments selected on the fly. *Nat. Chem.* **2020**, *12*, 945–951.
- (9) Behler, J. Representing potential energy surfaces by high-dimensional neural network potentials. *J. Phys. Condens. Matter* **2014**, *26*, 183001.
- (10) Brooks, B. R. et al. CHARMM: the biomolecular simulation program. *J. Comput. Chem.* **2009**, *30*, 1545–1614.

- (11) Larsen, A. H.; Mortensen, J. J.; Blomqvist, J.; Castelli, I. E.; Christensen, R.; Dułak, M.; Friis, J.; Groves, M. N.; Hammer, B.; Hargus, C.; others, The atomic simulation environment – a Python library for working with atoms. *J. Phys. Condens. Matter* **2017**, *29*, 273002.
- (12) Unke, O. T.; Brickel, S.; Meuwly, M. Sampling reactive regions in phase space by following the minimum dynamic path. *J. Chem. Phys.* **2019**, *150*, 074107.